Rock and Soil Mechanics

Volume 42 | Issue 2 Article 6

6-18-2021

Effect of sensor calibration on moment tensor analysis of granite uniaxial compression

Yi REN
Key Laboratory of Ministry of Education for Efficient Mining and Safety of Metal Mine, University of Science and Technology Beijing, Beijing 100083, China

Shun-chuan WU
Faculty of Land Resource Engineering, Kunming University of Science and Technology, Kunming, Yunnan 650093, China, wushunchuan@ustb.edu.cn

Yong-tao GAO
Key Laboratory of Ministry of Education for Efficient Mining and Safety of Metal Mine, University of Science and Technology Beijing, Beijing 100083, China

Yi-xiong GAN
Key Laboratory of Ministry of Education for Efficient Mining and Safety of Metal Mine, University of Science and Technology Beijing, Beijing 100083, China

Custom Citation

REN Yi, WU Shun-chuan, GAO Yong-tao, GAN Yi-xiong, . Effect of sensor calibration on moment tensor analysis of granite uniaxial compression[J]. Rock and Soil Mechanics, 2021, 42(2): 451-461.

Rock and Soil Mechanics 2021 42(2): 451−461 ISSN 1000−7598
https: //doi.org/10.16285/j.rsm.2020.5695 rocksoilmech.researchcommons.org/journal

Effect of sensor calibration on moment tensor analysis of granite uniaxial compression

REN Yi[1], WU Shun-chuan[1, 2], GAO Yong-tao[1], GAN Yi-xiong[1]

1. Key Laboratory of Ministry of Education for Efficient Mining and Safety of Metal Mine, University of Science and Technology Beijing, Beijing 100083, China
2. Faculty of Land Resource Engineering, Kunming University of Science and Technology, Kunming, Yunnan 650093, China

Abstract: Moment tensor inversion theory is an effective method to study the rock failure mechanism. However, the inversion results are prone to large errors, which can mislead the understanding of fracture mechanism. In order to achieve a better understanding of the generation process and the mechanism of the rock macro-fracture surface, we perform a location analysis of source events based on the uniaxial compression test of a granite sample, with the help of ultrasonic testing and acoustic emission monitoring. The events near the macro-fracture with small location errors are selected for moment tensor inversion. Then, we use the network calibration method to calibrate the sensors so that more accurate moment tensors can be obtained. The results show that the source event locations are in good agreement with the locations of the specimen's macro-fracture. After the sensors having been calibrated, there are a few noticeable observations. The inversion root-mean-square (RMS) errors of moment tensors reduce significantly. The distributions of events on the *T*-*k* plot and *P*/*T* axis plot become more concentrated. The shear component and the proportion of different types of events change accordingly. The distributions of strike, dip and rake angles of the events become more concentrated, which are in general consistent with the macro-fracture of the specimen. The tensile angles of some events change from negative to positive. The above results reasonably explain the failure process and mechanism of the specimen and highlight the importance of sensor calibration for the moment tensor inversion, which can be a useful tool to provide guidance and reference for a deeper understanding of rock failure mechanism.

Keywords: moment tensor inversion; failure mechanism; uniaxial compression; calibration; location

1 Introduction

Acoustic emission monitoring technology is an important method to study the initiation, development and coalescence of rock cracks. The monitoring work mainly consists of the identification and picking of the rupture signal, the location of the rupture source and the inversion of the rupture mechanism, etc. In the field of seismology, the advantages of the moment tensor inversion method have been well demonstrated in the studies of source damage mechanism[1−3]. Although differing in scale, the basic principles and research workflow of acoustic emission monitoring share similarities between seismology and rock mechanics study. Therefore, many researchers have attempted to apply the moment tensor inversion to studying the source mechanism of rock failure, and many have shown encouraging results[4−12]. To list a few, Grosse et al.[13] conduct Brazilian splitting, pull-out tests and compression tests in order to verify the accuracy of moment tensor inversion in studying the source mechanism of concrete sample fracture. The inversion results show excellent agreement with the experimental results. Graham et al.[14] compare the advantages and disadvantages of the first P-wave polarity method and the amplitude inversion method in the study of acoustic emission source mechanism. The results show the broad use of moment tensor inversion in studying laboratory rock brittle fracture. Aker et al.[15] present the moment tensor analysis in the triaxial compression test using sandstone sample containing horizontal borehole. The results show the solution of source mechanism is consistent with the observed macroscopic fracture surface. Based on the characteristics of acoustic emission, Liu et al. [16] use far-field P-wave moment tensor inversion and propose a novel moment tensor decomposition method to study the acoustic emission sources of granite under uniaxial compression. Huang[17] use the acoustic emission moment tensor inversion to study the three-point bending and Z-shape shear tests. The uniaxial loading tests of rock samples with circular hole, arched hole and double-sided hole are analyzed to study the failure mechanism of the rock.

Although moment tensor inversion has been extensively used in the studies of rock failure mechanism, there are many factors required to be considered to obtain accurate moment tensor results, including environmental noise, signal attenuation, the feasibility of medium model, and the coupling between the sensor and the sample, etc.

Received: 25 May 2020 Revised: 5 November 2020
This work was supported by the National Natural Science Foundation of China (51774020, 51934003) and the National Key Research and Development Program of China (2017YFC0805300).
First author: REN Yi, male, born in 1992, PhD candidate, mainly engaged in moment tensor analysis and rock mechanics experimental research.
E-mail: rymr0611@gmail.com
Corresponding author: WU Shun-chuan, male, born in 1969, PhD, Professor, mainly engaged in teaching and research on geotechnical engineering and mining engineering. E-mail: wushunchuan@ustb.edu.cn

The inversion of moment tensor with large errors are highly likely to mislead the interpretation of the source mechanism, and therefore make unreasonable conclusions. Regarding to these factors, researchers have made many attempts to improve the moment tensor inversion process, and one important conclusion is that the calibration of sensor can effectively improve the inversion accuracy [8, 18–21]. At present, there are mainly three ways to estimate the sensor calibration coefficient: the pencil-lead break test method[18], the ultrasonic calibration method[19], and the network calibration method[20–21]. Grosse et al.[18] use the pencil-lead break test during the concrete block experiment in order to obtain the relative calibration coefficient of each sensor, and they have applied those coefficients to the calculation of moment tensor. This type of calibration method is usually carried out after the sensor has been installed, and before the start of mechanical test. For uniaxial compression samples, no matter where the pencil-lead break test is performed on the sample, the distances between each sensor and the lead break will always be different. In addition, the incidence angle of waves generated by lead break to the sensors varies. Therefore, errors can occur during the amplitude correction, which makes the obtained calibration coefficients less accurate. Kwiatek et al.[19] use ultrasonic testing technology to calibrate the sensors in the laboratory rock experiments. The results show that after the sensor calibration, the moment tensor inversion error (measured by RMS) of the seismic source becomes smaller, and the distribution of the seismic sources in the *T-k* plot becomes more concentrated. However, this calibration method requires the incidence angles to be distributed relatively uniformly in the range of 0° to 90°. Each incident angle refers to the angle between the ray path and the normal direction of each ultrasonic sensor. Only when the uniform distribution is met, the method can construct a reasonable amplitude correction model, and therefore solve the relative magnitude of each sensor's calibration coefficient. At the same time, the method needs to re-calculate those coefficients for each time or each stage of the ultrasonic testing results, which may result in limitations. Davi et al.[20] propose an alternative calibration method based on the nature of seismic source, namely the network calibration method, during their study of seismic moment tensor. They apply the method to laboratory rock mechanics experiments[21], and achieve the inversion results with smaller error (RMS). Correspondingly, the distribution of seismic sources in the *P/T* axis plot is more concentrated. This calibration method only needs to use the collected amplitude data of seismic source to perform a joint inversion, and by a few iterations the calibration coefficient can be solved in a robust way. In addition, this method has no requirement on the positioning of the sensors, which makes it convenient to use.

The studies discussed above have achieved meaningful results. Nevertheless, in laboratory rock mechanics experiments, there are insufficient studies discussing the influence of sensor calibration on source rupture types and source geometric parameters. Based on the previous work, this study focuses on the failure process of granite under uniaxial compression. We use ultrasonic acquisition and acoustic emission monitoring to locate acoustic emission events. We apply moment tensor inversion to the events near the macroscopic fracture surface of the sample, and we use the monitoring network calibration method[20–21] to calibrate the sensor. We compare and analyze the results before and after the use of sensor calibration, including the RMS error generated by the moment tensor inversion, *T-k* plot, *P*/*T* axis plot, source decomposition and classification, and source geometric parameters. The comparison and analysis should help further understand the rock failure process and fracture mechanism, which provides further guidance for the research on laboratory rock failure and acoustic emission.

2 Moment tensor inversion and the theory of sensor calibration

There are three commonly used moment tensor inversion methods to solve the source mechanism: the full waveform inversion method, the amplitude inversion method, and the first P-wave polarity method. Eyre et al. [22] give a comprehensive review of the three methods, and the advantages and disadvantages are summarized as follows. The first P-wave polarity method is simple and efficient to use, but this method can be easily limited by factors such as the location of the sensor and the type of seismic source. For example, when the locations of sensors are relatively concentrated in a certain position with respect to the event, inversion results may not be obtained accurately. The full waveform inversion method is a relatively accurate method. However, the inversion process is computationally expensive. It is also greatly affected by the medium model and velocity model. At the same time, the method achieves better inversion results in low-frequency data, whereas the performance is less stable when handling high-frequency data. In comparison, the amplitude inversion method does not suffer that computational burden, and it can also achieve accurate results in a controllable environment. In theory, both P- and S-wave can be used for amplitude inversion. However, the identification and picking of S-wave usually give higher uncertainty, which makes it less applicable in laboratory experiments. The first P-wave amplitude inversion is more common. This paper is also based on that method.

The theories of the first P-wave amplitude inversion and network calibration method mainly include

$$\boldsymbol{u} = \boldsymbol{G}\boldsymbol{m} \tag{1}$$

where $\boldsymbol{G}$ is a $n\times6$ matrix containing the spatial derivatives of Green's function, which represents the medium information between the sensor and the seismic source. The matrix $\boldsymbol{G}$ is expressed as

$$\boldsymbol{G}=\begin{bmatrix}\boldsymbol{g}^{(1)}\\ \boldsymbol{g}^{(2)}\\ \cdots\\ \boldsymbol{g}^{(n)}\end{bmatrix}=\begin{bmatrix}G_1^{(1)} & G_2^{(1)} & G_3^{(1)} & G_4^{(1)} & G_5^{(1)} & G_6^{(1)}\\ G_1^{(2)} & G_2^{(2)} & G_3^{(2)} & G_4^{(2)} & G_5^{(2)} & G_6^{(2)}\\ \cdots & \cdots & \cdots & \cdots & \cdots & \cdots\\ G_1^{(n)} & G_2^{(n)} & G_3^{(n)} & G_4^{(n)} & G_5^{(n)} & G_6^{(n)}\end{bmatrix} \tag{2}$$

where $G_k^{(i)}$ is the matrix element representing Green's function for the *i*-th sensor. There are

$$\left.\begin{aligned} &G_1=G_{1,1},\ G_2=G_{2,2},\ G_3=G_{3,3}\\ &G_4=G_{2,3}+G_{3,2},\ G_5=G_{1,3}+G_{3,1}\\ &G_6=G_{1,2}+G_{2,1}\end{aligned}\right\} \tag{3}$$

where $G_{p,m}$ refers to the amplitude received by the sensor generated by the point force along the *p*-axis and the moment on the m-axis. $\boldsymbol{m}$ is a vector containing the 6 independent components of the moment tensor $\boldsymbol{M}$

$$\boldsymbol{m}=\begin{bmatrix}M_{11} & M_{22} & M_{33} & M_{23} & M_{13} & M_{12}\end{bmatrix}^{\mathrm{T}} \tag{4}$$

$\boldsymbol{u}$ is a $n\times1$ matrix, representing the effective first P-wave amplitude of different sensors or components; *n* is the number of the effective first P-wave amplitudes that can be obtained in a single event. For one component sensor, *n* is the number of sensors.

Suppose there are *n* sensors with known calibration coefficients, and we add a new sensor data with unknown calibration coefficient. This leads to

$$g^{(n+1)}\boldsymbol{m}=C^{(n+1)}u^{(n+1)} \tag{5}$$

where $C^{(n+1)}$ is the sensor calibration coefficient that needs to be solved.

Combining equations (1) and (5) gives

$$\begin{bmatrix}\boldsymbol{G} & 0\\ g^{(n+1)} & -u^{(n+1)}\end{bmatrix}\begin{bmatrix}\boldsymbol{m}\\ C^{(n+1)}\end{bmatrix}=\begin{bmatrix}\boldsymbol{u}\\ 0\end{bmatrix} \tag{6}$$

When there is only one calibrated sensor among *n* sensors, the emission of *S* acoustic events can give the total number of *Sn* equations. Among them, there are 6*S* unknown moment tensor elements need to be solved, and (*n*-1) unknown calibration coefficients need to be solved.

The solution of moment tensor requires at least 6 sensors. To improve the computational stability, suppose $n\geqslant8$, and suppose the number of acoustic emission events is not less than 10, that is, $S\geqslant10$, and the inequality $Sn>(6S+n-1)$ can be always established. In theory, the *Sn* identity calculation formula is a statically indeterminate problem. The more the number of sensors or the more acoustic emission sources, the more stable the calculated results will be. At the same time, even if the calibration coefficients of *n* sensors are all unknown, the moment tensor and sensor calibration coefficients can still be solved by using the network calibration method. However, in this situation, only the relative value of moment tensor and sensor calibration coefficients can be obtained, but the actual magnitude cannot be obtained. Since the study of seismic source in this paper only concerns the relative magnitude of the moment tensor components, and there is no relation to the absolute magnitude of the seismic source, the use of relative moment tensor and relative calibration coefficient can meet our requirements.

After solving the moment tensor, the decomposition result is also important. Different decomposition methods can draw different conclusions. In the field of source mechanism study, most work use the method proposed by Knopoff et al.[23] to decompose the moment tensor into isotropic (ISO) component, double-couple (DC) component, and compensated linear vector dipole (CLVD) component. For the details of decomposition please refer to Vavryčuk [24–25].

The study on the process and the type of rock failure requires the analysis of the geometric parameters of the fracture surface and the sliding vector. Two parameters are needed to describe the geometry of a plane, that is, the strike and the dip. Considering plane sliding, that is, the sliding vector is perpendicular to the plane normal vector, it requires an additional parameter, the sliding angle, to describe the direction of movement. Considering spatial sliding, that is, the sliding vector is not perpendicular to the plane normal vector, it requires another parameter, the crack angle, to describe the vector of motion. The definition of each geometric angle is illustrated in Fig. 1, where N refers to North, E refers to East, and D refers to Down. The relationship between the moment tensor $\boldsymbol{M}$, the normal vector $\boldsymbol{n}$ and the sliding vector $\boldsymbol{v}$ can be simply expressed as

$$\boldsymbol{n}=\sqrt{\frac{M_1-M_2}{M_1-M_3}}\boldsymbol{e}_1+\sqrt{\frac{M_3-M_2}{M_3-M_1}}\boldsymbol{e}_3 \tag{7}$$

$$\boldsymbol{v}=\sqrt{\frac{M_1-M_2}{M_1-M_3}}\boldsymbol{e}_1-\sqrt{\frac{M_3-M_2}{M_3-M_1}}\boldsymbol{e}_3 \tag{8}$$

respectively, where $M_1\geqslant M_2\geqslant M_3$ and they are the eigenvalues of the moment tensor $\boldsymbol{M}$; $\boldsymbol{e}_1$, $\boldsymbol{e}_2$ and $\boldsymbol{e}_3$ are the corresponding eigenvectors, respectively. The normal vector $\boldsymbol{n}(n_1,\ n_2,\ n_3)$ of the fracture surface and the sliding vector $\boldsymbol{v}(v_1,\ v_2,\ v_3)$ have the geometric relations with the strike angle φ, dip angle δ, sliding angle γ and crack angle α, which can be written as

$$n_1=-\sin\delta\sin\varphi \tag{9}$$

$$n_2=\sin\delta\cos\varphi \tag{10}$$

$$n_3=-\cos\delta \tag{11}$$

$$v_1=\left(\cos\gamma\cos\varphi+\cos\delta\sin\gamma\sin\varphi\right)\cos\alpha-\sin\delta\sin\varphi\sin\alpha \tag{12}$$

$$v_2=\left(\cos\gamma\sin\varphi-\cos\delta\sin\gamma\cos\varphi\right)\cos\alpha+\sin\delta\cos\varphi\sin\alpha \tag{13}$$

$$v_3=-\sin\gamma\sin\delta\cos\alpha-\cos\delta\sin\alpha \tag{14}$$

It is worth mentioning that when using Eqs. (9) to (14) to solve the geometric angle of the source, two different rupture surfaces will be obtained. One is the actual source rupture surface, and the other is the auxiliary surface. The relation between the two is that the normal vector $\boldsymbol{n}$ and the sliding vector $\boldsymbol{v}$ of the actual source rupture surface are the sliding vector $\boldsymbol{v}'$ and the normal vector $\boldsymbol{n}'$ of the auxiliary surface, respectively. Kao et al.[26] present the three-point bending test of granite and they discuss that the normal vector $\boldsymbol{n}$ of the actual source rupture surface should be parallel or close to the direction of the minimum principal stress undertaken by the rock sample. According to this theory, considering the uniaxial compression test, the normal vector of the actual rupture surface should be close to horizontal, that is, the source dip angle should be close to 90°. This can be a reference to identify the actual source rupture surface, and therefore obtain the corresponding strike and sliding angle.

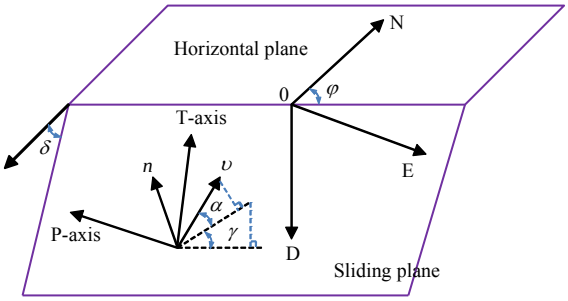

Fig. 1 Schematic diagram of the geometric parameters of the fracture

3 Experiment design

3.1 Sample preparation and loading method

The research target of this experiment is granite. The samples are cylindrical granite with a diameter of 50 mm, a height of 100 mm, and a density of 2.647 g/cm^3. The processing accuracy meets the ISRM requirements[27].

As shown in Fig. 2(a), we use the GAW-2000 microcomputer-controlled electro-hydraulic servo rigidity testing machine to apply loading to samples. The experiment applies the loading at a rate of 0.2 kN/s and ensures the quasi-static loading condition until the sample is broken. The upper and lower ends of a sample are added with anti-friction materials, which consist of a double-layer polytetrafluoroethylene (PTFE) with the middle smeared with butter, as shown in Fig. 2(b).

3.2 Acoustic emission monitoring

The monitoring are undertaken by the InSite acoustic emission signal acquisition system of ITASTA company and the Nano30 sensor of American Physical Acoustics Company (PAC). The InSite acoustic emission signal acquisition system uses a PAD amplifier unit with a built-in bandpass filter of approximately 100 kHz to 1 MHz, which can amplify the original acoustic signal with a gain of 30 to 70 dB, and then transmits and saves

(a) Servo rigidity testing machine (b) Installation of sensors

Fig. 2 Loading equipment and attached sensors

the signal. The sampling frequency of the device is 10 MHz. The resolution of waveform digitization is 16 bit. The Nano30 sensor has a diameter of about 8 mm, and an operating frequency range of 125 to 750 kHz. In addition, the device has the functionality of emitting and receiving ultrasonic active seismic source signals. The pulse generator interface unit (PIU) can generate a 500 V high-voltage pulse in each sensor in order, which acts as the active seismic source signal, and the other sensors serve as the receiving end to collect the corresponding signals in turn. For the details of the experiment please also refer to the listed studies [28–29]. By using the active seismic source measurement technology, the wave velocity under each propagation path can be measured during the rock sample loading process, so that we can obtain more accurate measurements to locate the acoustic emission events. Accurate location results are important to the inversion of source moment tensor and the understanding of source mechanism. The hardware InSite acoustic emission signal acquisition system is supported by its corresponding software InSite_Lab, which can realize the functions including signal pick-up, event locating and source mechanism inversion, etc.

In this experiment, 12 acoustic emission sensors are evenly distributed on the surface of the sample, so there is no space to monitor the circumferential strain of the sample. During the experiment, since all the sensors are shared by the acoustic emission monitoring and the ultrasonic active seismic test, the work of the two needs to be performed alternately. We collect the data one time every minute from the ultrasonic active seismic source, which takes about 6 s. During this time, acoustic emission monitoring suspends its collection of data. We apply silicone grease between the acoustic emission sensor and the rock sample, and use a fixture to fix them. The locations of the sensors are illustrated in Fig. 3, and one photograph of the layout is given in Fig. 2(b).

4 Results analysis

4.1 Fracture

Four groups of experiments are carried out with similar conditions, of which three groups have shown approximately vertical macro fracture surfaces. The resultant fractures are similar, and one group is shown for detailed description (Fig. 4).

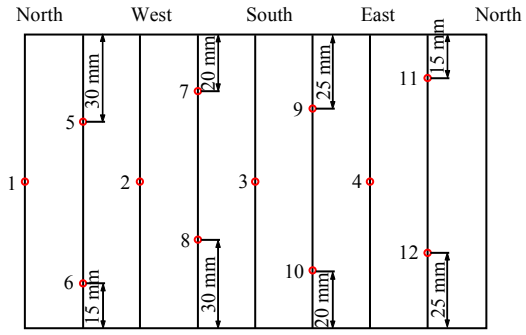

Note: Numbers 1 – 12 denote the sensor number ID

Fig. 3 Schematic diagram of sensors layout

(a) West-East view of sample (b) Top view of sample

Fig. 4 Photographs of the fractured surface of rock sample

During the experiment, a big sound can be heard from the sample when the load reaches about 120 kN. The experiment is stopped after the macro fracture surface of the sample can be observed with the naked eye. After the experiment, the sample is not completely split into two parts, in contrast, partial connection still exists in the lower part of the sample. The result of the sample fracture is shown in Fig. 4. The macroscopic fracture surface is in general parallel to the axis of the sample, with an inclination angle of about 90°. The strike of the fracture surface is roughly along the directions of N20° E and S20° W.

4.2 Ultrasonic measurement results

We process the monitoring data collected from the ultrasonic active seismic source, and obtain the P-wave velocity change following the paths between the sensors. For this analysis, we only select the propagation paths that pass through the central axis of the sample, and the repeated path is not considered (that is, path S01-S03 and path S03-S01 are identical, and only one is selected). The results are shown in Fig. 5.

As shown in Fig. 5, the P-wave velocity measured from path S05-S09 is the lowest, and the variation of the measurements is also small. Nevertheless, the last test shows a significant decline, and the decline is also the largest compared to other paths. Under normal conditions, during the initial stage of uniaxial compression, the P-wave velocity may either increase or decrease slowly in the horizontal or nearly horizontal direction inside the sample (paths S01-S03, S02-S04, S05-S09, S06-S10, S07-S11, and S08-S12). However, the P-wave velocity on the propagation path that close to the axial direction of the sample (paths S05-S10, S06-S09, S07-S12, and S08-S11) will increase significantly. Considering the measurements between the 8th and 9th ultrasonic active source tests, most propagation paths show different degrees of decrease of wave velocity, except for the propagation paths S06-S09 and S08-S12. The fact shows that there are obvious fracture surfaces in the areas where these paths cover. The wave velocities of the paths S06-S09 and S08-S12 keep increasing, which shows that the fracture surface has not developed into these two propagation paths.

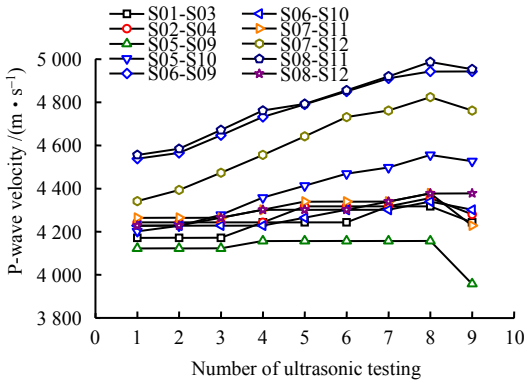

Fig. 5 P-wave velocity measurement along each path of the ultrasonic tests

4.3 Acoustic emission characteristics and source location results

Figure 6 shows the variation in axial force, ultrasonic testing, the acoustic emission event rate and the total number of events during the test.

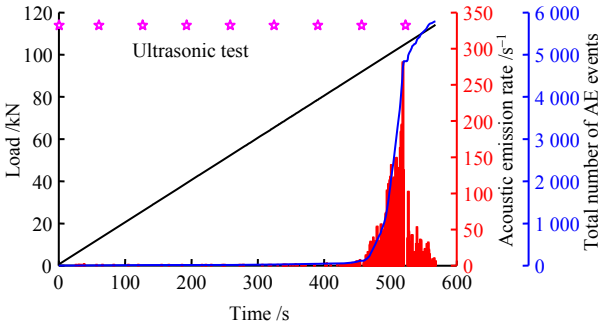

Fig. 6 Test load, acoustic emission event rate, and total number of acoustic emission events

Based on the obtained P-wave velocities of each path, we construct a time-varying transverse isotropic velocity model and use the collapsing grid search algorithm to locate the seismic source. We obtain a total of 5793 acoustic emission positioning events. The event distribution is shown in Fig. 7.

As observed from the time sequence and spatial location of each event, the initial development of the macroscopic fracture surface appears near the top of the sample. The fracture surface gradually expands to the bottom of the sample over time. This observation is consistent with the variation of P-wave velocity

obtained by the ultrasonic testing results. Since the experiment has been stopped after the sound when the macro fracture happens, the sample is not completely split into two. Therefore, acoustic emission events are less observed near the bottom of the sample, and the effective positioned events are mainly distributed around the upper part.

Comparing the results with the sample fracture shown in Fig. 4, the positioning of acoustic emission events is general consistent with the appearance of the macroscopic fracture surface of the sample. The positioning results should be reasonable.

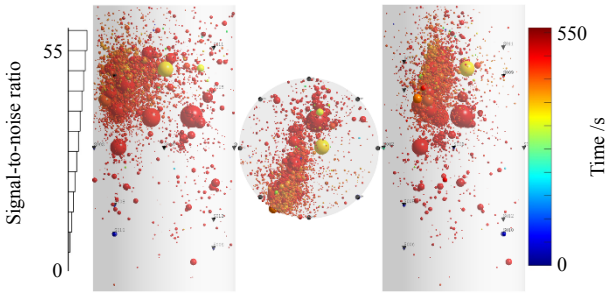

(a) South-North view (b) Top view (c) West-East view

Fig. 7 Results of locations of acoustic emission events

4.4 Calibration of sensor

In order to understand the generation and mechanism of the macroscopic fracture surface of the sample, we select specific events that meet the three criteria to perform our moment tensor analysis: 1) events are near the fracture surface; 2) events are collected by all the 12 sensors with effective first P-wave amplitude; and 3) the location error of the event is less than 2 mm. The equation that calculates the event location error is given as

$$E_{\mathrm{RMS}} = V_{\mathrm{p}} \sqrt{\sum_{i=1}^{N} \Delta T_i \Big/ N} \tag{15}$$

where E_{RMS} is the location error; V_{p} is the P-wave velocity model; ΔT_i is the absolute difference between the theoretical arrival time and the actual measured time from the source to the sensor i; and N is the number of sensors used to locate an event.

As a result, there are in total 644 acoustic emission events being selected that meet the criteria. The moment tensor analysis is based on a homogeneous velocity model, where the P-wave velocity is chosen as 4 500 m/s. The temporal and spatial distributions of the selected events are shown by Fig. 8.

Since we are interested in a relative calibration, the values of the calibration coefficients can be scaled up and down by the same factor without affecting the moment tensor calculation. To achieve a unique solution, we normalize the calibration coefficients so that the mean absolute value of all the sensor coefficients can be 1. The workflow of calibration mainly includes two major steps. First is to obtain the initial calibration coefficient of each sensor. Second is to solve the final calibration coefficient by an iterative method. Considering the first step, the workflow of solving the initial coefficients mainly includes the steps described as follows:

(1) We first assume that the sensor S01 has the calibration coefficient as 1. Since it is a relative calibration method, it is reasonable to select any sensor as a reference and set its calibration coefficient to 1. By substituting the amplitudes of all the events into Eqs. (1)– (6), the calibration coefficients of sensors S02–S12 can be solved. The calibration coefficients of all the sensors are then normalized to obtain C_k^i, where i is the sensor number between S02 to S12 that the calibration coefficient needs to be solved, and k is the number of the sensor with the assumed calibration coefficient, that is, S01 in this case.

(2) We then assume the calibration coefficient is 1 for each sensor from S02 to S12, respectively. We iteratively repeat the solution process described in step (1) and obtain another 11 groups of C_k^i. In the end, each sensor can obtain 12 calibration coefficients, and its initial calibration coefiicient C_0^j is the mean value of those, where j is the sensor number ID.

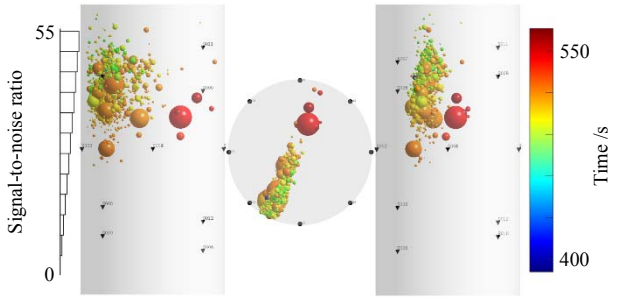

(a) South-North view (b) Top view (c) West-East view

Fig. 8 Selection of acoustic emission events for moment tensor inversion

The workflow of solving the final sensor calibration coefficients mainly includes:

(1) Based on the initial calibration coefficients C_0^j, we use the theory of jackknife test and assume again that the calibration coefficient of sensor S01 is unknown, whereas the coefficents of S02–S12 are the solved initial calibration coefficients. By substituting the amplitudes of all the events into Eqs. (1)– (6), a new calibration coefficient of sensor S01 can be obtained.

(2) We then assume the calibration coefficients of the sensors from S02 – S12 are unknown, respectively, and the other corresponding sensor coefficients are the solved initial coefficients. By using Eqs. (1)–(6), we can obtain a new set of calibration coefficients, which are then normalized and written as C_1^j, where j is the sensor number.

(3) Take C_1^j as the initial calibration coefficients and repeat the steps (1) and (2), we can obtain another new set of coefficients C_2^j. This forms a loop. Use C_2^j as the initial calibration coefficients and iteratively repeat this process, we can obtain C_n^j, where n is the number of iterations.

(4) The iteration can be stopped when the difference between the two groups of calibration coefficients C_n^j

and C_{n-1}^{j} is small enough. C_n^j is the final calibration coefficient.

A parameter λ_n^j is used to determine whether to terminate the loop or not, which is defined as the ratio of the sensor calibration coefficients between the two subsequent iterations, that is

$$\lambda_n^j = C_n^j / C_{n-1}^j \tag{16}$$

If λ_n^j is close to 1, it indicates the calculated calibration coefficients are essentially unchanged during the two iteration steps, and the calibration results are therefore converged.

The InSite_Lab software does not have the in-built function of network calibration. Therefore, we use MATLAB programming to undertake the workflow of moment tensor calculation and sensor calibration. The required results for calculation, including source location results and the first P-wave amplitudes, etc., all come from the software InSite_Lab. We use an iteration number of 25 for the sensor calibration. The variation of λ_n^j during the iterations and the final calibration results are shown in Fig. 9.

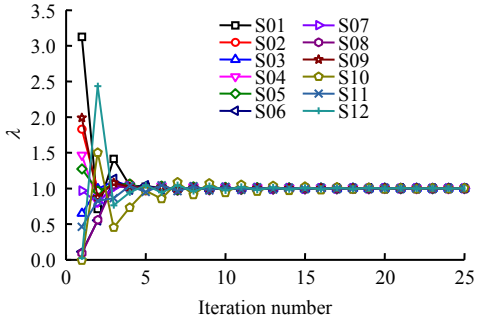

(a) Variation of λ during the iterative calibration

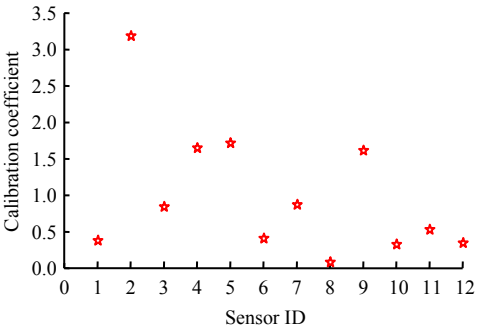

(b) The final calibration coefficients

Fig. 9 Plot of sensor calibration process and the final calibration coefficient

As shown in Fig.9(a), after 15 iterations, the calibration coefficients of all the sensors tend to converge. Figure 9(b) shows that the calibration coefficients of the five sensors, S01, S06, S10, S11, and S12, are relatively close. Although these values are small, they do not affect the analysis of the entire monitoring system. The main reason for the small calibration coefficients of the 5 sensors is that the coefficient of S02 is large. Because of the use of normalization, it is possible to produce large differences between each sensor calibration coefficient.

In this test, the deviation of the sensor calibration coefficient from 1 is mainly contributed by the following reasons:

(a) Environmental noise is different for each sensor.

(b) The degree of coupling is different between the sample surface and each sensor.

(c) During the test, the macroscopic fracture surface of the sample develops close to part of the sensors or even directly passes through the locations of some sensors. This leads to an increase of uncertainty in the waveform received by the sensor. For example, the sensor S08 has been affected and its final calibration coefficient is very close to 0 or even negative. If a sensor calibration coefficient is calculated as negative, we should consider abandoning the sensor and its measurements.

4.5 Moment tensor analysis

Without sensor calibration, the calculation of moment tensor uses the first P-wave amplitude data collected by the software InSite_Lab. After the calibration, we multiply the first P-wave amplitude by the corresponding calibration coefficients, and use them to calculate the moment tensor again. This result is then the inversion result including the sensor calibration. Except for the amplitude, the rest of the data and parameters involved in the moment tensor calculation remain the same with and without the sensor calibration.

To compare the difference of calculated moment tensor results with and without sensor calibration, we give the analysis of the two scenarios based on multiple perspectives and metrics.

First, in order to check the quality of the moment tensor inversion results, we use the normalized root mean square (RMS) difference between the acquired amplitude and the theoretical amplitude [8, 19–21] as the criterion to evaluate the inversion results quantitatively. The equation for calculating the RMS difference is given as

$$\mathrm{RMS} = \frac{\sqrt{\sum_{i=1}^{N}\left(A_i^{\mathrm{obs}} - A_i^{\mathrm{theor}}\right)^2}}{\sqrt{\sum_{i=1}^{N}\left(A_i^{\mathrm{obs}}\right)^2}} \tag{17}$$

where i is the sensor number ID; N is the number of sensors; A_i^{obs} is the measured amplitude of the i-th sensor; A_i^{theor} is the theoretical amplitude of the i-th sensor. After solving the moment tensor of the i-th event using the measured amplitude, the theoretical amplitude can be solved by using the corresponding forward algorithms.

As shown by Fig. 10, without sensor calibration, the RMS of each event is basically distributed uniformly between 0.1 and 1.0. There are 38% of the events with the RMS higher than 0.5. The mean value is 0.464. The maximum is higher than 1.1. With the use of sensor calibration, the RMS of most events can be reduced to less than 0.5. There are only 14% of the events with the RMS higher than 0.5. The mean value is 0.333. The maximum does not exceed 0.9. Therefore, the accuracy of the moment tensor inversion is greatly improved after the sensor calibration.

The *T*-*k* plot[30] can show the overall rupture type of acoustic source in a straightforward way. The obtained *T*-*k* plots with and without sensor calibration are shown in Fig. 11.

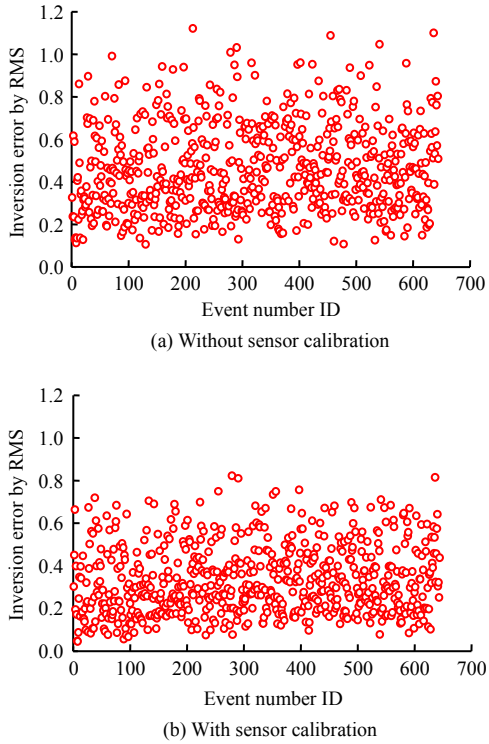

Fig. 10 Results of moment tensor inversion error (RMS) before and after calibration

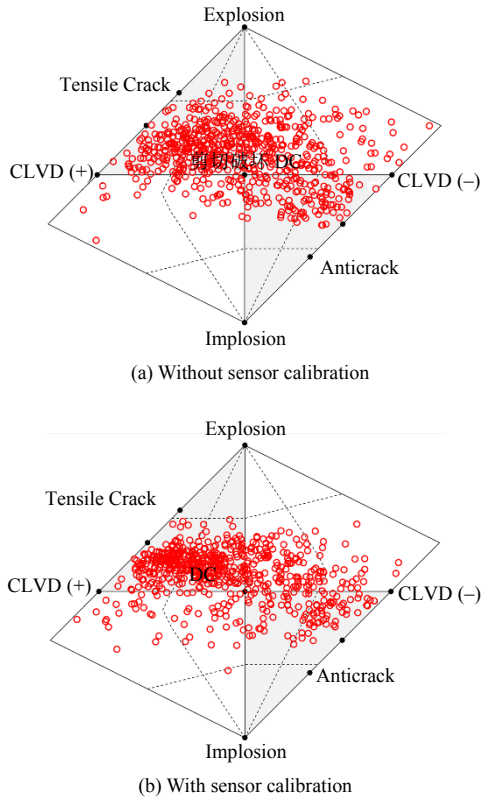

Fig. 11 *T*-*k* plots before and after calibration

As illustrated by Fig.11, the results with and without sensor calibration both show that most of the acoustic emission events have larger tension components and less compression and shear components. Without sensor calibration, the component ratios of events are more scattered, whereas with the calibration, the component ratios are more concentrated. This observation is consistent with the study given by Kwiatek et al.[19].

The *P*/*T* axis distribution diagram is useful when aim to illustrate the stress state and geometric form of the acoustic emission event. It is often used as a simple and quick tool to judge the inversion effect. The *P*/*T* axis plots with and without sensor calibration are shown in Fig. 12.

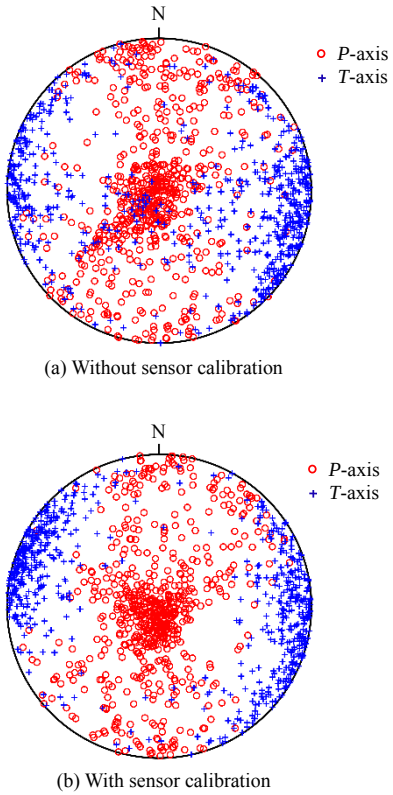

Fig. 12 *P*/*T* axis plots before and after calibration

As shown in Fig. 12(a), the resultant directions of *P*-axis and *T*-axis without sensor calibration are less confident. The events show a relatively scattered distribution. Although a general trend is seen, it is not certain. After the sensor calibration, the *P*/*T* axial distribution of the events becomes more concentrated. This comparison is consistent with the result shown by Davi et al. [21] The main observations are discussed as follows. Most of the events are compressed along the vertical direction, that is, the *P*-axis, which are mainly distributed around the center of the circle. This is consistent with the actual force that applied to the sample. The tension of the acoustic events, that is, the *T*-axis, is mainly following the direction within the range N60° W–N80° W and N60° E–S30° E. Although the two directional intervals are not completely symmetrical, they are basically normal to the macroscopic fracture surface. The force analysis of the macroscopic fracture

should be reasonable. There is a small number of events showing scattered *P*/*T* axial locations. The main reason is the heterogeneity inside the sample making the direction of the force between the particles different. This results in the fact that micro-cracks can have different geometry compared with the macroscopic fracture. However, the number of this type of distributed events is small, which does not affect the analysis of the macroscopic fracture surface.

By decomposing the moment tensor into 3 components (isotropic ISO, pure double couple DC, and compensated linear vector dipole CLVD), we can obtain the percentage of each component for each event with and without sensor calibration. Since the shear component (pure double couple DC) is used by many studies [29, 31] to quantify the source type, our analysis also focuses on the results of this component. The decomposition result is shown in Fig.13.

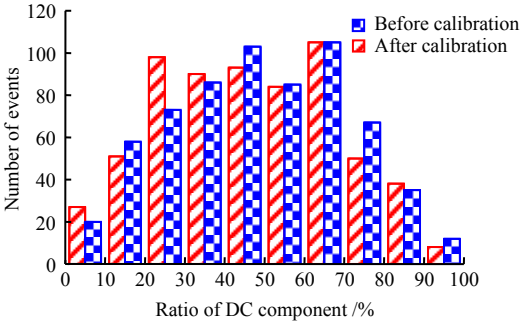

Fig. 13 Statistics results of DC components of moment tensor decomposition before and after calibration

As shown in Fig. 13, the DC component of the source has decreased after sensor calibration. Ohtsu [31] proposed to quantify the rupture type of acoustic source based on the proportion of the DC component P_{DC} in the moment tensor, where $P_{DC} \geqslant 60\%$ is defined as shear rupture, $P_{DC} \leqslant 40\%$ is defined as tensile rupture, and $40\% < P_{DC} < 60\%$ is defined as mixed rupture. According to this criterion, Table 1 shows the classification results: after sensor calibration, the proportions of shear events and mixed vents have decreased, whereas the proportion of tensile events has increased.

Table 1 Event classification before and after calibration

Classification of events	Without calibration /%	With calibration /%
Tensile events	36.8	41.3
Mixed events	29.2	27.5
Shear events	34.0	31.2

Figure 14 shows the geometric angles (strike, dip, sliding and crack angles) of the acoustic source with and without calibration. As seen in Fig.14, sensor calibration makes the distributions of strike, dip and slip angles more concentrated. At the same time, it pushes the distribution of crack angle moving towards the positive direction.

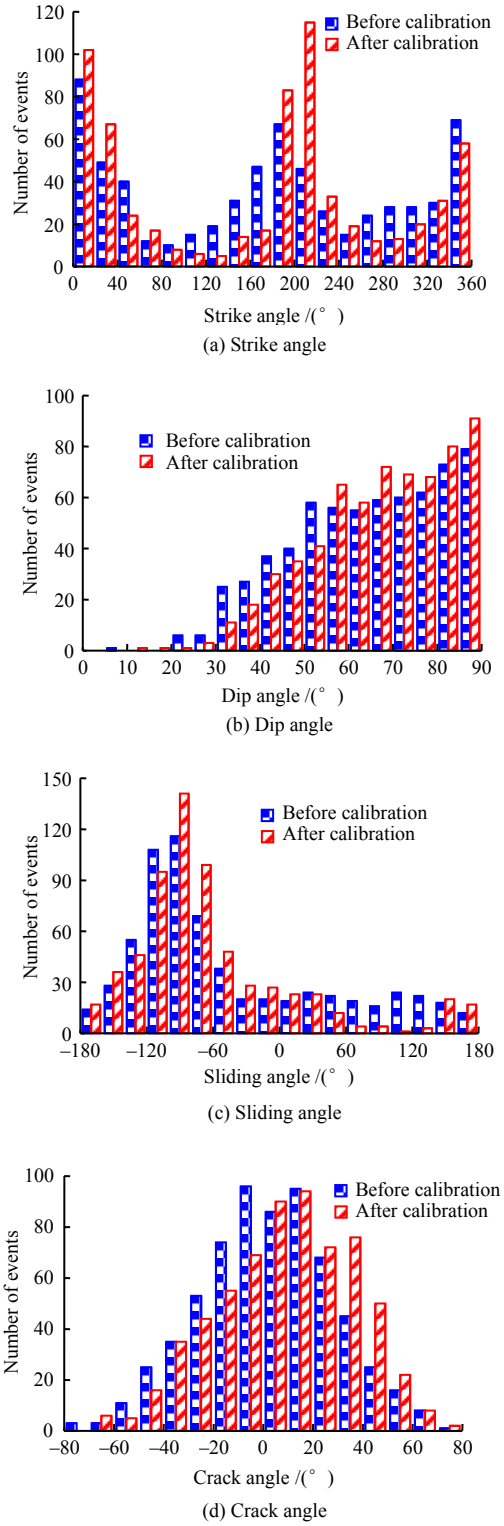

Fig. 14 Results of geometric parameters of acoustic emission events before and after calibration

A detailed analysis of the calculation results after sensor calibration can bring up the following discussion. The strike angles of the events are mainly distributed around the directions of N20° E and S20° W. The dip angle is mainly between 60° and 90° . The sliding angles of most events are around –90° , that is, around the vertical downward direction. The crack angles are relatively evenly distributed between –40° and 60° . The observations above show that the fracture surface

of all the events is roughly parallel to the vertical direction, with the strike around N20° E and S20° W, which is consistent with the geometric parameters that obtained from the macro-fracture surface of the sample. In addition, during the process until the appearance of macro-fracture surface, the sliding surface of each event has the tendency to be misaligned in the vertical direction, which is accompanied by the simultaneous development of tensile, mixed, and shear events. Tensile event accounts for the largest proportion.

5 Conclusion

(1) In the uniaxial compressional acoustic emission monitoring experiment, the inversion results of moment tensor with large errors are highly possible to mislead the understanding of the source. This is especially obvious when the conclusions are based on the quantitative RMS analysis and the qualitative *T*-*k* plot and *P*/*T* axial plot.

(2) The network calibration method can improve the moment tensor inversion results effectively. It results in a smaller RMS and a more concentrated source distribution in the *T*/*k* plot and *P*/*T* axial plot. The geometric parameters of the source are more closely related to those of the macroscopic fracture surface.

(3) Tensile, mixed and shear events co-exist during the process of developing of the macroscopic fracture surface, which is approximately parallel to the axis of applying the uniaxial compression for this test. Among the three types of events, tensile events accounts for the largest proportion.

(4) Based on the quantitative analysis of the geometric parameters of the seismic source, we can achieve a better understanding of the geometry of the marco-fracture surface (by strike and dip) as well as the displacement of the fracture (by sliding and crack angle). This provides an important tool for a deeper understanding of the rock failure process and its related mechanisms.

Acknowledgements:

Thanks to Professor Vavryčuk Václav from the Institute of Geophysics of the Czech Academy of Sciences for his support and guidance on the calibration code of the acoustic emission sensor.

References

[1] AKI K, RICHARDS P G. Quantitative seismology[M]. Sausalito California: University Science Books, 2002.

[2] CERVENY V. Seismic ray theory[M]. New York: Cambridge University Press, 2005.

[3] WU Shun-chuan, HUANG Xiao-qing, CHEN Fan, et al. Moment tensor inversion of rock failure and its application[J]. Rock and Soil Mechanics, 2016, 37(Suppl.1): 1–18.

[4] ZANG A, CHRISTIAN WAGNER F, STANCHITS S, et al. Source analysis of acoustic emissions in Aue granite cores under symmetric and asymmetric compressive loads[J]. Geophysical Journal International, 1998, 135(3): 1113–1130.

[5] SELLERS E J, KATAKA M O, LINZER L M. Source parameters of acoustic emission events and scaling with mining-induced seismicity[J]. Journal of Geophysical Research: Solid Earth, 2003, 108(B9). DOI: 10.1029/2001JB000670.

[6] THOMPSON B D, YOUNG R P, LOCKNER D A. Premonitory acoustic emissions and stick‐slip in natural and smooth-faulted Westerly granite[J]. Journal of Geophysical Research: Solid Earth, 2009, 114(B2). DOI: 10.1029/2008JB005753.

[7] MANTHEI G. Characterization of acoustic emission sources in a rock salt specimen under triaxial compression[J]. Bulletin of the Seismological Society of America, 2005, 95(5): 1674–1700.

[8] STIERLE E, VAVRYČUK V, KWIATEK G, et al. Seismic moment tensors of acoustic emissions recorded during laboratory rock deformation experiments: sensitivity to attenuation and anisotropy[J]. Geophysical Supplements to the Monthly Notices of the Royal Astronomical Society, 2016, 205(1): 38–50.

[9] TANG Li-zhong, JIAN Ying-hua, LI Di-yuan, et al. Analysis of damage mechanism for surrounding rock based on microseismic moment tensor[J]. Rock and Soil Mechanics, 2017, 38(5): 1436–1444.

[10] GAN Yi-xiong, WU Shun-chuan, REN Yi, et al. Evaluation indexes of granite splitting failure based on RA and AF of AE parameters[J]. Rock and Soil Mechanics, 2020, 41(7): 2324–2332.

[11] LIU Jian-po, LIU Zhao-sheng, WANG Shao-quan. Analysis of acoustic emission source mechanisms for tensile and shear cracks of rock fractures[J]. Journal of Northeastern University (Natural Science), 2015, 36(11): 1624–1628.

[12] CHAI Jin-fei. Study on fracture mechanism of brittle rock based on moment tensor[D]. Beijing: University of Science and Technology Beijing, 2017.

[13] GROSSE C U, FINCK F. Quantitative evaluation of fracture processes in concrete using signal-based acoustic emission techniques[J]. Cement and Concrete Composites, 2006, 28(4): 330–336.

[14] GRAHAM C C, STANCHITS S, MAIN I G, et al. Comparison of polarity and moment tensor inversion methods for source analysis of acoustic emission data[J]. International Journal of Rock Mechanics and Mining Sciences, 2010, 47(1): 161–169.

[15] AKER E, KÜHN D, VAVRYČUK V, et al. Experimental

investigation of acoustic emissions and their moment tensors in rock during failure[J]. International Journal of Rock Mechanics and Mining Sciences, 2014, 70: 286–295.

[16] LIU Pei-xun, CHEN Shun-yun, GUO Yan-shuang, et al. Moment tensor inversion of acoustic emission[J]. Chinese Journal of Geophysics, 2014, 57(3): 858–866.

[17] HUANG Wen-bai. Research on acoustic emission source mechanisms of rock failure based on moment tensor theory[D]. Shenyang: Northeastern University, 2013.

[18] GROSSE C, OHTSU M. Acoustic emission testing[M]. Berlin, Heidelberg: Springer, 2008.

[19] KWIATEK G, CHARALAMPIDOU E M, DRESEN G, et al. An improved method for seismic moment tensor inversion of acoustic emissions through assessment of sensor coupling and sensitivity to incidence angle[J]. International Journal of Rock Mechanics and Mining Sciences, 2014, 65: 153–161.

[20] DAVI R, VAVRYČUK V. Seismic network calibration for retrieving accurate moment tensors[J]. Bulletin of the Seismological Society of America, 2012, 102(6): 2491–2506.

[21] DAVI R, VAVRYČUK V, CHARALAMPIDOU E M, et al. Network sensor calibration for retrieving accurate moment tensors of acoustic emissions[J]. International Journal of Rock Mechanics and Mining Sciences, 2013, 62: 59–67.

[22] EYRE T S, VAN DER BAAN M. Overview of moment-tensor inversion of microseismic events[J]. The Leading Edge, 2015, 34(8): 882–888.

[23] KNOPOFF L, RANDALL M J. The compensated linear-vector dipole: a possible mechanism for deep earthquakes[J]. Journal of Geophysical Research, 1970, 75(26): 4957–4963.

[24] VAVRYČUK V. Inversion for parameters of tensile earthquakes[J]. Journal of Geophysical Research: Solid Earth, 2001, 106(B8): 16339–16355.

[25] VAVRYČUK V. Tensile earthquakes: theory, modeling, and inversion[J]. Journal of Geophysical Research: Solid Earth, 2011, 116(B12): B12320.

[26] KAO C S, CARVALHO F C S, LABUZ J F. Micromechanisms of fracture from acoustic emission[J]. International Journal of Rock Mechanics and Mining Sciences, 2011, 48(4): 666–673.

[27] ULUSAY R. The ISRM suggested methods for rock characterization, testing and monitoring: 2007-2014[M]. [S. l.]: Springer, 2014.

[28] WU Shun-chuan, GUO Pei, ZHANG Shi-huai, et al. Study on thermal damage of granite based on Brazilian splitting test[J]. Chinese Journal of Rock Mechanics and Engineering, 2018, 37(Suppl.2): 8–19.

[29] ZHANG S, WU S, ZHANG G, et al. Three-dimensional evolution of damage in sandstone Brazilian discs by the concurrent use of active and passive ultrasonic techniques[J]. Acta Geotech, 2020, 15: 393–408.

[30] HUDSON J A, PEARCE R G, ROGERS R M. Source type plot for inversion of the moment tensor[J]. Journal of Geophysical Research: Solid Earth, 1989, 94(B1): 765–774.

[31] OHTSU M. Acoustic emission theory for moment tensor analysis[J]. Research in Nondestructive Evaluation, 1995, 6(3): 169–184.